

Determination of Band Curvatures by Angle-Resolved Two-Photon Photoemission in Thin Films of C₆₀ on Ag(111)

Steven T. Shipman,[†] Sean Garrett-Roe, Paul Szymanski,[‡] Aram Yang, Matthew L. Strader, and Charles B. Harris*

Chemistry Department, University of California-Berkeley, Berkeley, California 94720, and Chemical Sciences Division, E. O. Lawrence Berkeley National Laboratory, Berkeley, California 94720

Received: September 6, 2005; In Final Form: November 22, 2005

The thickness-dependent interfacial band structure was determined for thin films of C₆₀ on Ag(111) by angle-resolved two-photon photoemission spectroscopy. Dispersions of molecular-orbital derived bands (HOMO, LUMO+1, and LUMO+2) were acquired, and limits were placed on their possible effective masses. A group theoretic approach is also incorporated to further understand the properties of these states. The HOMO, LUMO+1, and LUMO+2 bands possess (best-fit) effective masses of $-7 m_e$, $-7 m_e$, and $-12 m_e$, respectively. These values are consistent with theoretical calculations, averaged over the closely spaced subbands for each state, and provide practical limits on the effective fundamental charge-transport properties of C₆₀ films.

Introduction

Epitaxial thin films of C₆₀ grown on metal substrates have received considerable attention in recent years as a model system for the study of molecular electronic devices.^{1–4} This system is ideal for a number of reasons: among them are the ease of preparation of high-quality mono- and multilayers, the rich electronic structure of the fullerenes, and the wealth of prior experimental and theoretical work on this system.

A number of photoemission studies have previously been performed on thin films of C₆₀^{5–17} and alkali-doped C₆₀.^{18–22} Of these studies, those particularly relevant to the current manuscript are those by Ton-That et al.,¹⁷ Yang et al.,²⁰ and Brouet et al.²¹ Each of these papers examines angle-resolved photoemission spectra of C₆₀ on Ag(111), but unlike the current paper, they are primarily concerned with photoemission only from a C₆₀ monolayer, and furthermore, as they all utilize one-photon techniques, only characterize initially occupied states. It has only been relatively recently that the technique of angle- and time-resolved two-photon photoemission (2PPE) has been applied to study C₆₀ films.^{23–26} The advantage of a two-photon technique over other photoemission techniques (such as ultra-violet photoelectron spectroscopy or inverse photoelectron spectroscopy) lies in the fact that it can simultaneously probe both initially occupied as well as initially unoccupied electronic band structure, and that it can do so with an ultrafast temporal resolution.

Two-photon photoemission is a pump–probe technique for exploring the properties of interfacial electronic states. Initially unoccupied states as studied by 2PPE are illustrated in Figure 1. Electrons from below the Fermi level (E_F) of a metal substrate (or from an initially occupied surface²⁷ or adsorbate²⁸ state) are excited into an intermediate state with a pump pulse, $h\nu_1$. This intermediate may be “virtual” in the case of an initially occupied state. The probe pulse $h\nu_2$ then photoemits the excited-state

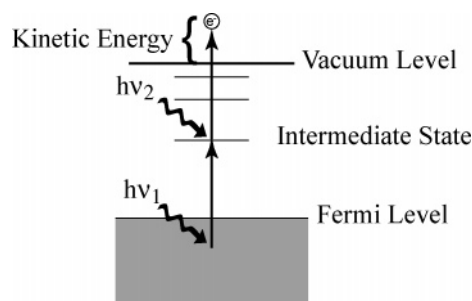


Figure 1. Schematic depiction of the two-photon photoemission process. A pump pulse, $h\nu_1$, excites an electron from below the Fermi level into an initially unoccupied intermediate state. A probe pulse, $h\nu_2$, arrives at some delay time later and excites the electron above the vacuum level. By measuring the kinetic energy of the photoemitted electron and knowing the energies of $h\nu_1$ and $h\nu_2$, the energy of the intermediate state may be referenced to the vacuum level.

electron by giving it energy greater than the vacuum level, E_{vac} . The binding energy of the unoccupied electronic states can be calculated by measuring the kinetic energy, E_{kin} , of the photoemitted electrons and then subtracting the energy of the probe pulse photon. This experiment may be performed in a time-resolved fashion, by delaying the probe pulse with respect to the pump pulse.

Two-photon photoemission can also be used as a probe of two-dimensional band structure by taking spectra as a function of the angle of the surface normal relative to the detector. In angle-resolved 2PPE, the objective is to determine the electronic band dispersion (E_{kin} vs the momentum $\hbar k_{\parallel}$ parallel to the interface) of an interfacial state along a particular crystal direction. For an interface possessing long-range order, the parallel momentum of an electron is conserved during photoemission and is related to E_{kin} via

$$k_{\parallel} = \sqrt{\frac{2m_e E_{\text{kin}}}{\hbar^2}} \sin \theta \quad (1)$$

where m_e is the free electron mass and θ is the detection angle from surface normal. The band dispersion is typically

* Corresponding author: cbharris@berkeley.edu.

[†] Department of Chemistry, University of Virginia, Charlottesville, VA 22904.

[‡] Current address: Department of Chemistry, Brookhaven National Laboratory, Upton, NY 11973.

fit to a parabolic function

$$E_{\text{kin}} = E_0 + \frac{(\hbar k_{\parallel})^2}{2m^*} \quad (2)$$

where E_0 is the energy at the band minimum and m^* is an effective electron mass. Nearly free (delocalized) electronic states have values of $|m^*| \approx m_e$, while spatially localized electronic states have apparent values of $|m^*| \gg m_e$.

A large value of m^* is necessary but not sufficient for an electronic state to be localized. In the case of a localized electronic state, the measured large effective mass is a result of the fact that k_{\parallel} is not a good quantum number, and such states may be described as a superposition of plane waves with different values of k_{\parallel} . In this case, measurements as a function of θ simply select the different k_{\parallel} components of the superposition, and E_{kin} is constant as a function of angle. It is possible, however, for a delocalized electron to have a large value of m^* . Note that the estimate of m^* is based on the assumption of a parabolic or cosine-like band structure. In general, such a function will not be a true representation for the band as a whole; however, such estimates should be valid quantities in the vicinity of the Γ point ($k_{\parallel} = 0$).

Angle-resolved 2PPE spectra were taken of thin films of C_{60} on Ag(111) in order to probe the fundamental charge-transport properties of these films. Dispersions of the molecular-orbital derived states were fit to values of m^* . These results are then compared to theoretical predictions of the electronic band structure.

Experimental Section

2.1 Ultrafast Laser System. Details of our laser system, constructed by Coherent, Inc., have been published elsewhere and are described here only briefly.²⁹

Our overall laser system is pumped by two Coherent Verdi pump lasers. The Verdis are diode-pumped, continuous-wave Nd:YVO₄ lasers with intracavity lithium triborate doubling crystals producing 532 nm output. A Coherent Mira 900-F Ti:sapphire oscillator is pumped by a Verdi V-5 laser operating at 5.5 W, and a Coherent RegA 9000 regenerative amplifier is pumped by a Verdi V-10 laser operating at 10.5 W.

The Mira operates at 76 MHz and 800 nm and is optimized for mode-locked operation with a bandwidth of 10–13 nm full width at half-maximum, preferably 12 nm or higher. A small portion of the output, approximately 50 mW average power, is regeneratively amplified by the RegA, operating at 200 kHz. The RegA output is used to pump a Coherent OPA (optical parametric amplifier) unit, which generates white light continuum as well as the 400 nm second harmonic. Parametric amplification of a portion of the continuum allows for the generation of tunable visible light from 470 to 740 nm. The OPA output (visible beam) is compressed to a wavelength-dependent value of 70–120 fs via dispersion compensation (bluer wavelengths are closer to 120 fs), after which a portion of the beam is frequency doubled (UV beam). The remainder of the OPA output is delayed in time (positively or negatively) with respect to the doubled beam via a Klinger translation stage.

In the experiments described herein, visible photon energies range from 2.1 to 2.4 eV and the UV photon energies range from 4.2 to 4.8 eV. Typical pulse energies are 4.2 nJ for the visible beam and 2.1 nJ for the UV beam. Both beams are focused to a spot no smaller than 100 μm in radius, resulting in upper limits on the fluences of 13.4 and 6.7 $\mu\text{J}/\text{cm}^2$ for the visible and UV beams, respectively. These low fluences are

deliberately used in order to minimize the effects of space-charge broadening on the 2PPE spectra; on average, one electron is photoemitted for every ten pairs of pulses for the clean surface at zero pump–probe delay.

2.2 Ultrahigh Vacuum Chamber. Our metal substrate is a single crystal of Ag(111), 99.999% pure, obtained from MaTeCK GmbH. The crystal is mounted on a manipulator arm which allows for the rotation of the surface normal of the crystal about a fixed point, in addition to the standard whole-crystal translations and rotations to face various viewports and instruments in the chamber. The crystal is wedged, adding to the maximum angular range provided by the surface-normal goniometer. The wedge angle was determined to be 6.0° from the minimum energy in the dispersion of the image states on the clean surface, allowing for the surface normal to be rotated from −3.5° to +26.0°. The Ag(111) crystal is oriented such that dispersion measurements are taken along the Γ -X direction, although LEED indicates that the crystal is slightly misaligned by approximately 9°.

The Ag(111) crystal is kept in a UHV chamber with a base pressure on the order of 1×10^{-10} Torr. The crystal is connected to a Janis ST-400 continuous flow cryostat capable of using liquid nitrogen or helium, achieving a base temperature of approximately 125 K with nitrogen and 50 K with helium. Photoelectrons are captured by a time-of-flight detector. Additionally, the chamber is outfitted with an SRS RGA300 quadrupole mass spectrometer for residual gas analysis, a LEED and Auger system (Omicron SPECTALEED) for assessing the quality and composition of thin films on the substrate, a precision leak valve for introducing various gases into the chamber, and an ion gun for Ar⁺ sputter cleaning of the surface. Auger spectra are recorded using software provided by Omicron, and LEED images are captured via an EHD KAMPro02 CCD camera (EHD Imaging GmbH). The vacuum chamber is also connected via a gate valve to a smaller chamber, referred to as the molecular beam epitaxy (MBE) chamber.

The MBE chamber has a base pressure on the order of 1×10^{-9} Torr and is equipped with a small furnace (Applied EPI low temp K-cell with PBN crucible) capable of heating source material up to 1300 K with ± 0.1 K stability. The crucible-to-substrate distance is ~ 34 cm, and a pinhole of 1 cm diameter is located immediately before the gate valve (21 cm before the sample) to minimize contamination of the 2PPE chamber.

The C_{60} used in this study was obtained from Strem at a purity of 99.9%, and was placed into the MBE chamber without further purification, where it was thoroughly degassed prior to use. Similar to what was observed on Cu(111),²³ multilayers of C_{60} on Ag(111) may be removed from the surface by simply heating the crystal above 450 K, but C_{60} monolayers on Ag(111) resist our “standard” Ar⁺ sputter and anneal cycle (a 0.5 keV Ar⁺ sputter for 20 min at 500 K, followed by annealing the substrate for 20 min at 725 K), requiring instead an initial higher-energy sputter cycle for 10 min at 1.5 keV and 500 K, followed by a normal sputter and anneal cycle. After this procedure, LEED, Auger, and 2PPE indicate that the Ag(111) surface is clean.

Results

3.1 C_{60} Layer Growth: Calibration and Characterization. According to previous reports,²³ highly ordered C_{60} thin films are a prerequisite for observing sharp image states and narrow photoemission peaks. Consequently, before investigating the ultrafast electron dynamics of these films, some time was spent perfecting their growth. Thin films of C_{60} on Ag(111) are more like those on Au(111) rather than those on Cu(111); the

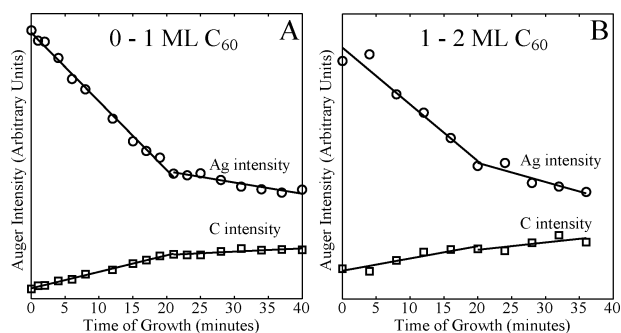


Figure 2. (a) Monitoring the growth of a 0–1 ML C_{60} film by Auger. Preparation conditions are a substrate temperature of 613 K and an MBE cell temperature of 683 K. (b) Monitoring the growth of a 1–2 ML C_{60} film by Auger. Preparation conditions are a substrate temperature of 400 K and an MBE cell temperature of 673 K.

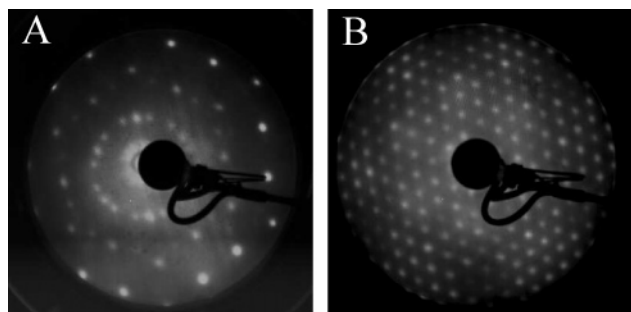


Figure 3. (a) LEED pattern taken at 32.0 eV of a 1 monolayer C_{60} film. The $(2\sqrt{3} \times 2\sqrt{3})R30^\circ$ phase is the majority phase, but spots corresponding to the minority $R \pm 14^\circ$ phases are present as well. (b) LEED pattern taken at 54.0 eV of a 10 monolayer C_{60} film.

equilibrium film structure on Ag(111) and Au(111) is a $(2\sqrt{3} \times 2\sqrt{3})R30^\circ$ structure, rather than the 4×4 structure seen on Cu(111).³⁰ Consequently, the dosing parameters were adjusted to find the conditions reported by Tzeng et al.³⁰ as resulting in high-quality thin films (elevated substrate temperature during deposition and a slow growth rate of 0.05 monolayers/min).

The C_{60} coverage was calibrated via Auger spectroscopy, by examining the intensities of the C peak³¹ at 272 eV and the Ag primary peaks at 351–356 eV as a function of dosing time. When a slope change is observed in both features, this is interpreted as the completion of a layer.³² For the monolayer, favorable conditions for growth were an MBE cell temperature of 683 K and a substrate temperature of 613 K. These conditions give a completed monolayer at approximately 23 min of dosing (Figure 2a). LEED of this layer (Figure 3a) shows that the $(2\sqrt{3} \times 2\sqrt{3})R30^\circ$ structure is the majority phase, although there are small amounts of the $R \pm 14^\circ$ phases present. These minority phases could unfortunately never be completely quenched by varying the dosing conditions.

The growth of the second monolayer was also calibrated via Auger (Figure 2b), with the objective of determining conditions for multilayer growth that enable highly crystalline films of the thermodynamic (rather than kinetic) domains to predominate. Unfortunately, it is very difficult to observe the slope change in the C peak for these coverages, and so the layer completion time was determined by the slope change observed in the Ag signal. The substrate temperature for multilayer growth was chosen to be 400 K, as it was observed that the second and higher monolayers slowly desorb at temperatures above 450 K. Auger indicated that the MBE cell temperature of 683 K used for the monolayer was slightly too high (slope change in approximately 18 min), and so the MBE cell temperature was

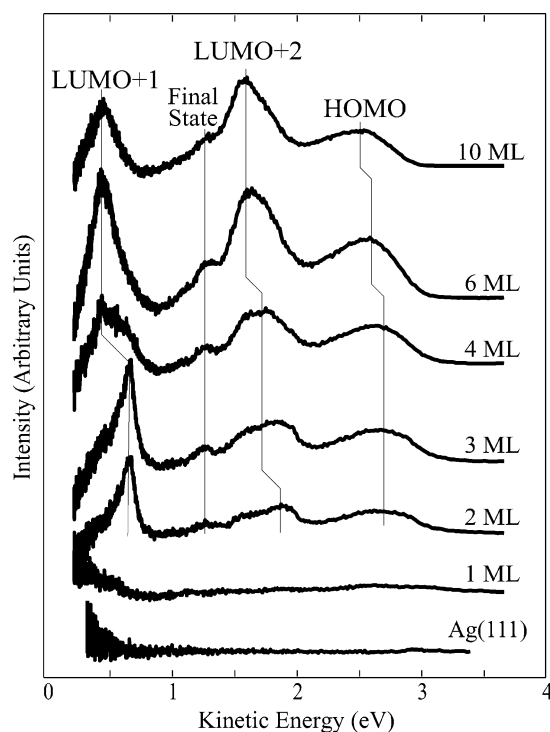


Figure 4. One-color 2PPE spectra of C_{60} layers of varying thickness, taken with both $h\nu_1$ and $h\nu_2$ equal to 4.78 eV energy. The spectrum corresponding to the Ag(111) substrate was acquired with photon energies of 4.58 eV; at 4.78 eV, one-photon photoemission would dominate the spectrum. The molecular orbital-derived states are labeled as such, and the feature labeled “Final State” corresponds to a final state resonance energetically located above the vacuum level. The lines indicate how the peak positions shift as a function of layer thickness.

lowered to 673 K for multilayer growth, yielding a slope change at approximately 20 min. A 20-minute dose at 673 K MBE cell temperature at a substrate temperature of 400 K was therefore determined to be the unit of multilayer dosing, and higher coverages were assigned based on this dosing time. LEED of the 10 monolayer coverage (Figure 3b) indicates that the multilayer films are highly crystalline and possess the expected structure.

3.2 2PPE Spectra. Films 1, 2, 3, 4, 6, and 10 monolayers (ML) thick of C_{60} were grown on a Ag(111) substrate. Substantial charge transfer from the metal substrate to the film occurs for the 1-ML coverage (on the order of 0.75 electrons per molecule³³), but subsequent layers remain electrically neutral. As such, spectra of the 1-ML film are substantially different from those of thicker films, which appear relatively similar regardless of coverage. Note that, to eliminate complications relating to possible glass transitions or polymerization in multilayer C_{60} films,^{16,34} all 2PPE was performed at temperatures of 80 K or below, and the sample was shielded from the femtosecond laser pulses until these temperatures were reached.

One-color (Figure 4) and two-color (Figure 5) 2PPE spectra of each C_{60} coverage exhibit several different peaks after background subtraction. For the one-color data, the background function accounts for contributions from inelastically scattered electrons, which can dominate the signal at low kinetic energies. The background function used was first described by Shirley³⁵ for photoemission from a gold substrate, and has also been applied in a study of photoemission from the sp band of Ag(111).³⁶ The background function for the two-color data is simply the spectrum of the one-color data at that coverage (i.e., the background is simply due to photoemission resulting from two interactions of the system with the UV photons).

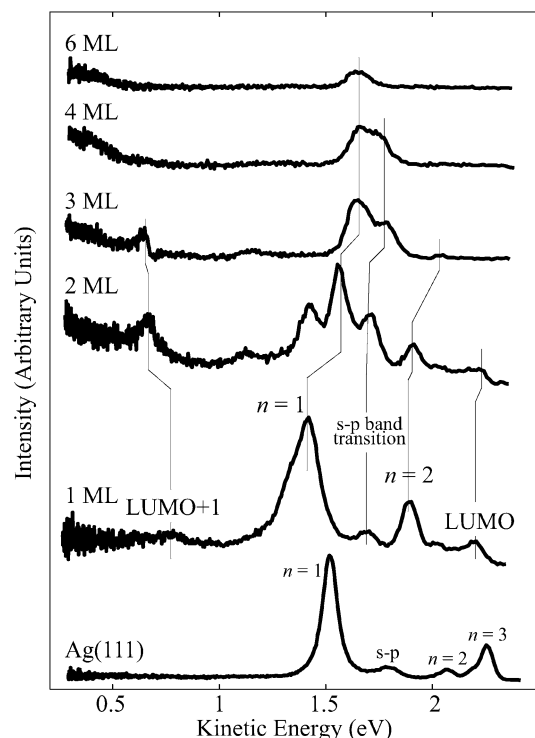


Figure 5. Two-color 2PPE spectra of C_{60} layers of varying thickness, taken with a UV photon energy of 4.78 eV and a visible photon energy of 2.39 eV. The spectrum corresponding to the Ag(111) substrate was taken with a UV photon energy of 4.58 eV and a visible photon energy of 2.29 eV; at a UV photon energy of 4.78 eV, one-photon photoemission would dominate the spectrum. The LUMO and LUMO+1-derived states from C_{60} and the sp bulk-band transition are labeled as such. The features labeled $n = 1$ and $n = 2$ (and $n = 3$ on the clean surface) correspond to image potential states. The lines indicate how peak positions shift as a function of coverage.

Two-color spectra were acquired only for films ≤ 6 ML thick, as two-color signal could not be obtained with thicker films. The reason for this is somewhat unclear, but the phenomenon is definitely dependent on layer thickness. In thick films where the signal was vanishingly small, it was found that partially desorbing the C_{60} (by flashing the substrate to temperatures in excess of 450 K) leads to an immediate recovery of signal. No such loss in signal with film thickness was observed for the one-color (UV–UV) data. We will return to a possible explanation for this after detailing the peak assignments.

To ascertain the identities of these peaks, wavelength surveys were undertaken in which the peak positions are examined as a function of the pump and probe photon energies. Systematic peak shifts with changes in photon energy give information about the number and time ordering of the system's interactions with the pump and probe photons, which can then be used to reference the different peaks to the Fermi or vacuum level. These data are plotted in Figure 6, and the energy level diagram resulting from these assignments is given in Figure 7.

The identities of the observed peaks are fairly clear from both reference to the existing C_{60} photoemission studies of Dutton and co-workers on Cu(111)^{23,24,25} and Au(111)²⁶ as well as the electronic structure of isolated C_{60} molecules.^{37,38,39} (Note that the peaks assigned as the C_{60} LUMO and LUMO+1 levels in ref 23 were subsequently reassigned as the LUMO+1 and LUMO+2 levels in ref 25. With these corrected assignments, the spectra shown in Figure 4 in this manuscript are analogous to those shown in Figures 5 and 6 of ref 23.) The observed features include image potential states, final state resonances

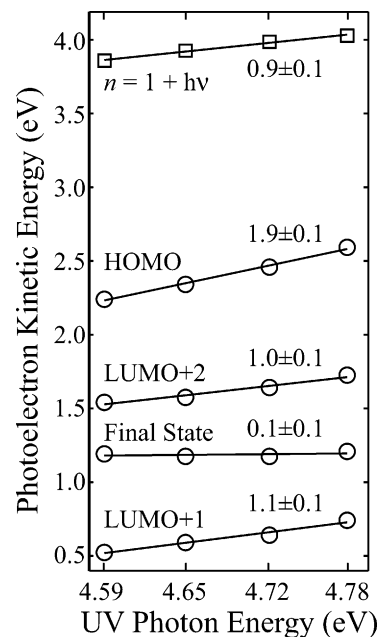


Figure 6. Plot of the photoelectron kinetic energy vs UV photon energy for several different features taken from the 3-ML C_{60} thin film. Each set of data is labeled with our assignment and the best-fit slope is indicated. Slopes of 0, 1, and 2 indicate final states, initially unoccupied states, and initially occupied states, respectively. Note that the $n = 1$ data (squares) were taken from two-color spectra; the points plotted are the kinetic energies from that data plus an additional visible photon energy (half the UV photon energy) to place the $n = 1$ feature where it would appear in a one-color spectrum.

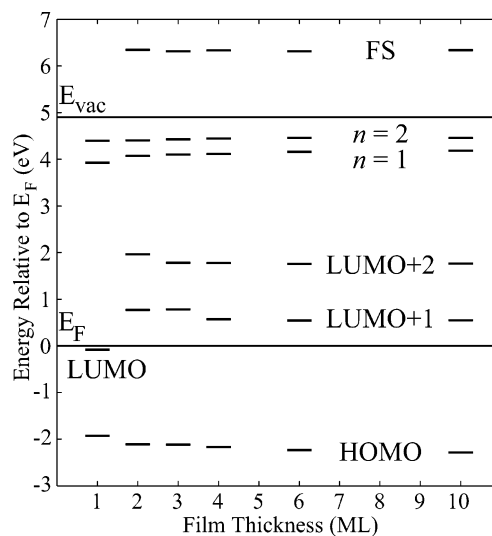


Figure 7. Position of the various observed energy levels as a function of C_{60} film thickness.

above the vacuum level, and states derived from C_{60} molecular orbitals. The properties of the molecular orbital-derived states will be the focus of the remainder of this manuscript; details of the other features will appear in a forthcoming paper.

Now that these states have been assigned, we can consider why the two-color spectra show a pronounced decrease in intensity with increasing film thickness while the one-color spectra do not. One possibility is that the C_{60} layers are somehow more effectively attenuating the visible light than the UV light (either by absorption or reflection). However, a rough calculation of Fresnel reflection and transmission coefficients and attenuation length using the frequency-dependent dielectric function for C_{60} ⁴⁰ indicates that the magnitude of these effects for films on

the order of six molecules thick should not be nearly as dramatic as the observed reduction in signal intensity. A more plausible argument relies on the notion, previously expressed by Dutton and co-workers,²⁵ that for thick films the photoemission signal primarily originates from the topmost few layers of the film. In this case, the idea is that even though the femtosecond pulses are still capable of interacting with the Ag(111) substrate, only those electrons excited near the vacuum-fullerene layer will be successfully photoemitted and detected due to escape depth arguments. This then implies that the only initial states to be considered are those within the C₆₀ layer. If only the C₆₀ electronic structure is accounted for, however, there is no route by which the visible pulse can populate the LUMO+1 level at the visible photon energies used in these experiments; the lowest energy transition capable of populating the LUMO+1 level is the HOMO–LUMO+1 transition at 2.7 eV, but the visible photon energies range only from 2.1 to 2.4 eV. The finite widths of these features might allow the transition to occur at the highest visible energies (from the high-energy tail of the HOMO to the low-energy tail of the LUMO+1, assuming homogeneous broadening), but the HOMO–LUMO+1 gap appears to increase with coverage (Figures 4 and 7). Furthermore, even if the LUMO+1 level were initially populated via a UV photon, it lies too far below the vacuum level to be photoemitted with a visible photon. If this explanation is correct, the decrease in two-color signal with film thickness is circumstantial evidence that the LUMO+1 feature discussed here is excitonic in nature.

Once the molecular-orbital derived states (HOMO, LUMO+1, and LUMO+2) were assigned, their dispersions were examined in the $\bar{\Gamma}$ – \bar{M} direction (a 30° rotation from the Ag-(111) direction due to the $(2\sqrt{3} \times 2\sqrt{3})R30^\circ$ structure of the C₆₀ overlayers). The overbars indicate that the dispersions being examined are those along a two-dimensional surface. Previous studies on fullerenes⁴¹ indicate that the escape depth for photoelectrons is roughly the size of a single C₆₀ molecule. In other words, the detected photoelectrons originate primarily from the topmost layer, a result corroborated by the work of Dutton and co-workers.²⁵ So, throughout the rest of this manuscript, we will be interpreting our dispersions as due to the dispersions of the electrons in the topmost C₆₀ layer, which considerably simplifies the analysis as compared to the full three-dimensional case.

The positions of the molecular-orbital-derived states are difficult to ascertain in the 1-ML film, and so dispersions from this coverage are not used in the estimates of m^* for these bands. For thicker films, the energetic positions of the bands change slightly as a function of coverage, but the effective masses of the bands appear to be independent of film thickness. It should be noted that these measured effective masses correspond to an average over the energetically degenerate or nearly degenerate subbands; we are unfortunately unable to resolve separate peaks for the 5-fold degenerate HOMO, 3-fold degenerate LUMO+1, or the 5-fold degenerate LUMO+2.

As it is experimentally difficult to distinguish between large values of m^* (the experimental observable, E_{kin} , varies as $1/m^*$, which changes slowly for large values of m^*), we report a range of effective masses for the HOMO, LUMO+1, and LUMO+2 bands, corresponding to our estimates from the data of the most likely values of m^* . Figure 8 shows this graphically. To plot data from multiple coverages on the same axes, the k_{\parallel} values were first determined from the measured kinetic energies, using eq 1. After the parallel momenta (and consequently the curvatures of the states) were determined, the data from each coverage were then offset by a constant energy in order to fit

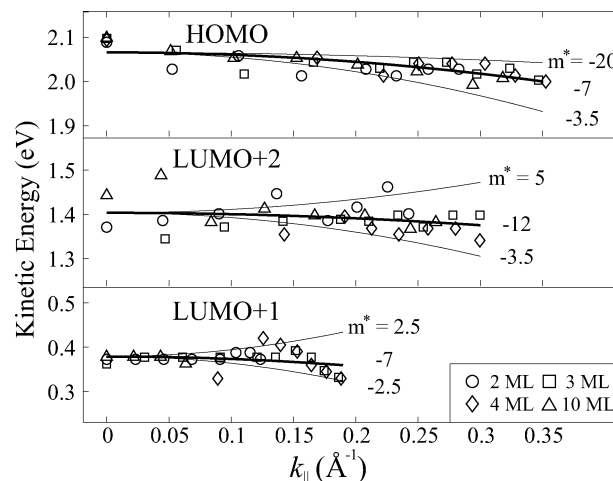


Figure 8. Dispersion data for the HOMO, LUMO+1, and LUMO+2 states in C₆₀ films 2, 3, 4, and 10 ML thick. The lines are possible fits to the effective mass of the band. For the HOMO level, the effective mass (in units of m_e) is expected to lie between -3.5 and -20 with a best fit value of -7 . For the LUMO+1 level, the effective mass is expected to lie between -2.5 and $+2.5$ with a best fit value of -7 , and for the LUMO+2 level, the effective mass is expected to lie between -3.5 and $+5$ with a best fit value of -12 .

TABLE 1: Upper and Lower Bounds and Best Fit Values of the Effective Mass (units of m_e) for the HOMO, LUMO+1, and LUMO+2 States

identity	m^* bounds	m^* best fit
HOMO	$-3.5 - -20$	-7
LUMO+1	$-2.5 - +2.5$	-7
LUMO+2	$-3.5 - +5$	-12

values of m^* to the full data set at once. These constant energy shifts essentially just account for the shift in band positions with film thickness seen in Figure 7.

As seen in Figure 8, the HOMO-derived band has a negative effective mass but the signs of the LUMO+1- and LUMO+2-derived masses are difficult to unambiguously determine, although the best fit values are negative in both cases. Table 1 shows the effective masses (ranges and best fit value) for the HOMO, LUMO+1, and LUMO+2 bands, using eq 2.

We should note that previous work has indicated that the presence of random orientational disorder can lead to an anomalously flat dispersion,⁴² but this is not expected to be an issue at the temperatures used here, as C₆₀ molecules below the rotational phase transition at approximately 90 K are expected to be predominately in one rotational orientation.^{43,44}

The effective mass (m^*) values estimated above for the HOMO, LUMO+1, and LUMO+2 bands in thin film C₆₀ are important parameters for understanding charge transport in these bands. The bandwidth, the magnitude of the energy difference between the top and bottom of the bands (proportional to $|1/m^*|$), is related to the extent of orbital overlap, and the sign of m^* indicates the presence or absence of nodes between nearest neighbors.⁴⁵ The nodal structure is dictated by the symmetry of the lattice and of the molecular orbital basis. If there is no node between identical replicas of the molecular orbital, then the effective mass will be positive; conversely, if there is a node, the effective mass will be negative.^{28,45}

As the signs of the dispersions for the LUMO+1 and LUMO+2 derived states are uncertain from the experimental data, a theoretical approach is desired in order to attempt to resolve this ambiguity. Two methods are taken. The first method is a “brute force” approach, involving a direct calculation of

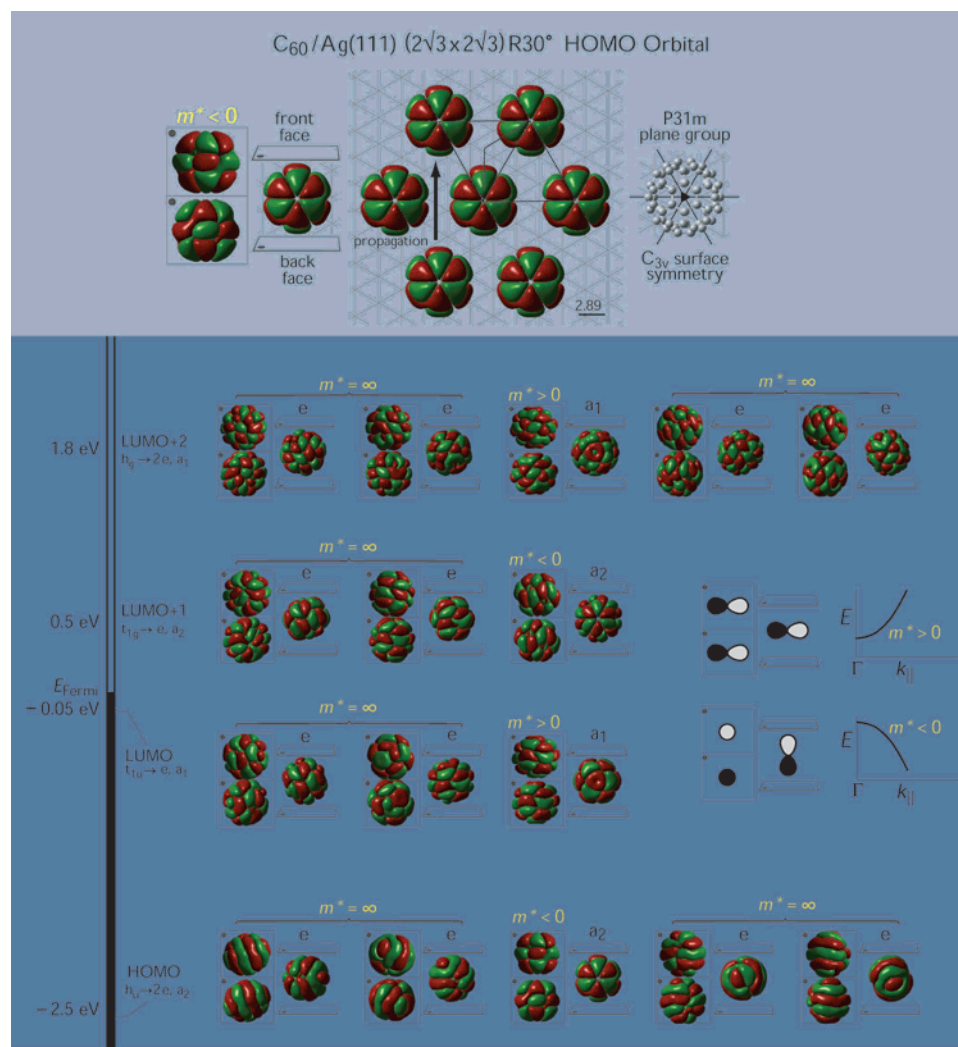


Figure 9. Top panel: One subband of the 5-fold degenerate HOMO is tiled on a Ag(111) lattice. This structure corresponds to the $P31m$ plane group, and the symmetry of the C_{60} is lowered from I_h to C_{3v} . The colors of the orbital indicate the sign of the wave function. The arrow indicates the $\bar{\Gamma}$ – \bar{M} direction, which connects the front face of one orbital with the back face of another. For the subband shown, the signs of the wave function are opposite over the entire face, corresponding to a node between the molecules at $k_{\parallel} = 0$, and consequently a negative effective mass. Bottom panel: Wave function visualizations for the HOMO, LUMO, LUMO+1, and LUMO+2 orbitals, along with expected curvatures of the states. The e , a_1 , and a_2 labels correspond to the symmetries of these wave functions in the C_{3v} point group. Inset: a schematic of the nodal structure for two simple cases, along with sketches of the dispersion for these cases.

the wave functions. The second method utilizes group theory to understand the symmetries of the orbitals along the $\bar{\Gamma}$ – \bar{M} direction.

To directly examine the orbitals, the HOMO, LUMO, LUMO+1, and LUMO+2 orbitals for isolated C_{60} molecules were calculated with Gaussian⁴⁶ at the RHF/STO-3G level of theory and visualized using Gaussview. The C_{60} molecules were then placed with hexagonal faces down on hcp sites of the Ag(111) lattice, in accord with recent calculations of the C_{60} orientation in the $(2\sqrt{3} \times 2\sqrt{3})R30^\circ$ phase on Ag(111).⁴⁷ Figure 9 shows the different HOMO, LUMO, LUMO+1, and LUMO+2 subbands, in addition to detailing how these orbitals are arranged on the Ag(111) lattice.

In Figure 9, the different colors of the orbitals represent the sign of the wave function. The direction of propagation ($\bar{\Gamma}$ – \bar{M}) connects the front face of one orbital with the back face of another. Therefore, if the front and back faces have opposite colors in the same spatial region, there is a node between them, and m^* is expected to be negative, as in the case of the orbital represented in the top panel. The pairs of orbitals in Figure 9 connected with curly braces transform as a pair and have a net flat curvature ($m^* = \infty$). To summarize this figure, the HOMO

and LUMO+1 orbitals should have net negative effective masses (averaged over the subbands which are not experimentally resolvable), and the LUMO and LUMO+2 orbitals should have net positive effective masses.

These results may also be understood in a more formal way with the aid of group theory. Specifically, examining the nodal symmetry of the front face of one orbital with the back face of another is identical to examining the character of the orbitals under a reflection through a plane which is perpendicular to the $\bar{\Gamma}$ – \bar{M} direction and which bisects the molecules. With this in mind, all that remains is to determine the symmetries of these states and examine how they transform under reflection.

Isolated C_{60} molecules are highly symmetric, belonging to the icosahedral point group, I_h . This group has 120 symmetry operations and a formidable character table. However, when C_{60} is placed on a surface, its overall symmetry is dramatically lowered due to the difference between the surface below and the vacuum above. In the following analysis, we consider a C_{60} molecule with a hexagonal face down on an hcp site of the Ag(111) lattice, as in Figure 9. A layer of C_{60} molecules in this orientation belongs to the $P31m$ plane group, and the symmetry of each molecule is reduced to C_{3v} . The dispersion direction

TABLE 2: Symmetries of the HOMO, LUMO, LUMO+1, and LUMO+2 Orbitals under the I_h and C_{3v} Point Groups, Their Characters under Reflection, and the Net Curvature of the Bands^a

identity	I_h	C_{3v}	σ	net curvature
HOMO	h_u	e, e, a_2	0, 0, -1	negative
LUMO	t_{1u}	e, a_1	0, +1	positive
LUMO+1	t_{1g}	e, a_2	0, -1	negative
LUMO+2	h_g	e, e, a_1	0, 0, +1	positive

^a Positive and negative curvatures correspond to positive and negative signs of m^* , respectively.

probed in our experiments corresponds to a high-symmetry direction, and the energetic curvature of the bands may be understood by considering their characters with respect to a reflection under C_{3v} symmetry. A character of +1 under this operation corresponds to the wave functions on the front and back faces possessing the same sign and a positive effective mass, while a character of -1 under this operation corresponds to the wave functions differing by a phase of 180°, and thereby having opposite signs and a negative effective mass.

The h_u HOMO, t_{1u} LUMO, t_{1g} LUMO+1, and h_g LUMO+2 orbitals of the I_h point group transform into combinations of a_1 , a_2 , and e states in the C_{3v} point group (Table 2). The a_1 , a_2 , and e states each have a different character under reflection, corresponding in our experiment to differing signs of m^* . The a_1 states have a +1 character (positive m^*) and the a_2 states have a -1 character (negative m^*) under reflection. But what of the e states, which possess a character of 0? The character of 0 implies that these states have neither a positive nor a negative dispersion, but instead have a rigorously flat dispersion, corresponding to $m^* = \infty$. While it may appear from Figure 9 that one of a pair has a positive dispersion and the other has a negative dispersion (see the e states of the HOMO), these states must be taken as pairs to fully span their two-dimensional representations, and, when proper linear combinations of them are taken, they must have a curvature of 0.

The type of analysis shown in Table 2 indicates that, from a symmetry standpoint, the HOMO and LUMO+1 orbitals are expected to have a net negative curvature, and the LUMO and LUMO+2 orbitals are expected to have a net positive curvature. However, for the initially unoccupied orbitals, this analysis may be too simplistic. It has been suggested²⁶ that the states assigned here as LUMO+1 and LUMO+2 may not be populated by charge transfer from the metal substrate (anions), but instead might be due to excitations on the molecules themselves (excitons). The dispersions of excitonic states would then entail the movement of a correlated electron-hole pair, rather than the movement of a single particle, which is an implicit assumption of the above analysis.

Fortunately, the group theoretic approach is readily extended to consider on-molecule excitons. These types of states can be represented by a direct product of the electron orbital and the hole orbital on a given C_{60} , and the symmetries of the resulting states can be analyzed as above. At the photon energies used in these experiments, the relevant excitons to consider are the HOMO-LUMO+1 and the HOMO-LUMO+2 excitons. (The HOMO-1-LUMO+1 exciton is not considered, as this is a dipole-forbidden transition.) The direct products corresponding to these excitons are

$$h_u \otimes t_{1g} = t_{1u} + t_{2u} + g_u + h_u \quad (3)$$

for the HOMO-LUMO+1 exciton, and

$$h_u \otimes h_g = a_u + [t_{1u}] + [t_{2u}] + [g_u] + g_u + 2h_u \quad (4)$$

for the HOMO-LUMO+2 excitons, where the braces indicate the antisymmetric product (triplet states). The different split states resulting from these direct products may then be considered as above, by examining how they behave under a lowering of the symmetry from I_h to C_{3v} , and, finally, using their characters under reflection to predict their effective masses.

The h_u and t_{1u} states should transform like the HOMO and LUMO levels in Table 2, respectively, while the g_u and t_{2u} states have to be manually decomposed with the aid of character tables. When the full analysis is performed on the singlet states of these two excitons, it is seen that the HOMO-LUMO+1 exciton should have a net positive effective mass, and the HOMO-LUMO+2 exciton should have a net negative effective mass (Table 3).

Unfortunately, a certain determination of whether the LUMO+1 and LUMO+2-derived features are due to molecular excitations (excitons) or charge transfer from the metal (anions) is not possible from the theory and experimental data presented here, particularly as the group theory says nothing about the relative energies of the excitonic sub-states. For instance, it is possible that not all 15 of the singlet HOMO-LUMO+1 combinations will be populated, and as such, the observed dispersion will be due only to the average over the populated states. Further calculations of these excited states, such as by a configuration interaction approach, would be needed to clarify this issue. Experimentally, the approach to determine if these states are excitonic or anionic in nature would be a wavelength-dependent study in which one can tune on or off molecular resonances; such resonances should not be present if the excitations are from the relatively flat density of states residing in the metallic substrate. The relatively congested nature of the C_{60} electronic levels may hinder this determination, but systems with a simpler electronic structure should be amenable to this approach.

TABLE 3: Symmetries of Singlet Components of the HOMO-LUMO+1 and the HOMO-LUMO+2 Excitons under the I_h and C_{3v} Point Groups, Their Characters under Reflection, and the Net Curvature of the Bands^a

identity	I_h	C_{3v}	σ	net curvature
HOMO-LUMO+1	t_{1u}	e, a_1	0, +1	positive
	t_{2u}	e, a_1	0, +1	positive
	g_u	e, a_1 , a_2	0, +1, -1	flat
	h_u	e, e, a_2	0, 0, -1	negative
	$t_{1u} + t_{2u} + g_u + h_u$	$5e + 3a_1 + 2a_2$	$5(0) + 3(+1) + 2(-1)$	positive (+1)
HOMO-LUMO+2	a_u	a_2	-1	negative
	g_u	e, a_1 , a_2	0, +1, -1	flat
	$2 h_u$	$2 \times e$, e, a_2	2×0 , 0, -1	negative
	$a_u + g_u + 2h_u$	$5e + 1a_1 + 4a_2$	$5(0) + 1(+1) + 4(-1)$	negative (-3)
	Net			

^a Positive and negative curvatures correspond to positive and negative signs of m^* , respectively. The numbers in the net curvature column do not correspond to predicted effective masses; they simply correspond to the number of remaining states if positive and negatively dispersing states are allowed to cancel.

Regardless of the excitonic or anionic qualities of the unoccupied orbitals probed in these experiments, it is clear that in studying the photoemission from the HOMO orbital that the dispersions should map exactly onto the above group theory and direct visualization routes, and this state does indeed have an unambiguously negative value of m^* .

Additionally, the LUMO level is actually partially occupied in the monolayer, and it does indeed have a positive dispersion (as predicted by its symmetry properties in C_{3v}) when examined in two-color 2PPE experiments (not presented here). However, this state lies close enough to the Fermi level that it quickly disperses above the high-energy cutoff, precluding any quantitative analysis.

As such, while the values of m^* presented for the LUMO+1 and LUMO+2 may not correspond to the motion of a single particle in a band, the estimated range of m^* for the HOMO (-3.5 to $-20 m_e$) should be correct, as this state is initially occupied and there are no questions of the exciton vs anion variety.

For all orbitals observed experimentally, it appears as if the different subbands do not disperse by more than the measured peak-width of approximately 500 meV for the HOMO level and 100 meV for the LUMO+1 and LUMO+2 orbitals. This is unfortunate, as otherwise we might be able to extract values of m^* for the different subbands. Instead, our measured dispersions correspond to movement of the center-of-energy of the band. The exact source of these relatively large peak widths is uncertain, but it has been suggested that they may be due to vibronic or phononic broadening.^{48,49} The small splitting between subbands is not just an issue for 2PPE; the overall coupling between orbitals on adjacent molecules will likely involve an average over the closely spaced levels unless chemical substitution or externally applied fields enhance the splitting. The measurements from 2PPE are thus appropriate for describing the ensemble-averaged properties of thin films, which are relevant to their performance in device applications.

Conclusions

Angle-resolved 2PPE spectra were taken of C_{60} thin films on Ag(111), and the resulting dispersions for the HOMO, LUMO+1, and LUMO+2 states were fit to an effective mass m^* . To evaluate the experimental data, both direct and group theoretic considerations of nodal structure along the Γ -M dispersion direction were made. For the HOMO, the subband nodal structure is consistent with our measured dispersion, and for the LUMO+1 and LUMO+2 levels, the bands have an apparent nearly flat dispersion, and theoretical considerations are not sufficient to determine whether these features are due to states involving molecular excitations or charge transfer from the metal substrate. Nevertheless, these results indicate that angle-resolved 2PPE can be used as a direct experimental probe of band structure in systems with quite complicated electronic energy levels. The ability to measure the dispersions of both initially occupied and initially unoccupied states as functions of layer thickness and preparation will likely be a valuable asset in understanding the performance of model molecular-electronic devices.

Acknowledgment. This work was supported by the Director, Office of Science, Office of Basic Energy Sciences, Chemical Sciences Division of the U.S. Department of Energy, under Contract No. DE-AC02-05CH11231. The authors acknowledge NSF support for specialized equipment used in the experiments described herein.

References and Notes

- (1) Das, R.; Kiley, P. J.; Segal, M.; Norville, J.; Yu, A. A.; Wang, L.; Trammell, S. A.; Reddick, L. E.; Kumar, R.; Stellacci, F.; Lebedev, N.; Schnur, J.; Bruce, B. D.; Zhang, S.; Baldo, M. *Nano Lett.* **2004**, *4*, 1079.
- (2) Hasobe, T.; Imahori, H.; Kamat, P. V.; Ahn, T. K.; Kim, S. K.; Kim, D.; Fujimoto, A.; Hirakawa, T.; Fukuzumi, S. *J. Am. Chem. Soc.* **2005**, *127*, 1216.
- (3) D'Souza, F.; Smith, P. M.; Zandler, M. E.; McCarty, A. L.; Itou, M.; Araki, Y.; Ito, O. *J. Am. Chem. Soc.* **2004**, *126*, 7898.
- (4) Segura, J. L.; Martin, N.; Guldi, D. M. *Chem. Soc. Rev.* **2005**, *34*, 31.
- (5) Ohno, T. R.; Chen, Y.; Harvey, S. E.; Kroll, G. H.; Weaver, J. H.; Haufler, R. E.; Smalley, R. E. *Phys. Rev. B* **1991**, *44*, 13747.
- (6) Lof, R. W.; van Veenendaal, M. A.; Koopmans, B.; Jonkman, H. T.; Sawatzky, G. A. *Phys. Rev. Lett.* **1992**, *68*, 3924.
- (7) Maxwell, A. J.; Brühwiler, P. A.; Nilsson, A.; Mårtensson, N.; Rudolf, P. *Phys. Rev. B* **1994**, *49*, 10717.
- (8) Magnano, E.; Vandr , S.; Cepek, C.; Goldoni, A.; Laine, A. D.; Curr , G. M.; Santaniello, A.; Sancrotti, M. *Surf. Sci.* **1997**, *377*, 1066.
- (9) Hesper, R.; Tjeng, L. H.; Sawatzky, G. A. *Europhys. Lett.* **1997**, *40*, 177.
- (10) Tsuei, K.-D.; Yuh, J.-Y.; Tzeng, C.-T.; Chu, R.-Y.; Chung, S.-C.; Tsang, K.-L. *Phys. Rev. B* **1997**, *56*, 15412.
- (11) Jacquemin, R.; Kraus, S.; Eberhardt, W. *Solid State Commun.* **1998**, *105*, 449.
- (12) Schwedhelm, R.; Kipp, L.; Dallmeyer, A.; Skibowski, M. *Phys. Rev. B* **1998**, *58*, 13176.
- (13) Quast, T.; Bellmann, R.; Winter, B.; Gatzke, J.; Hertel, I. V. *J. Appl. Phys.* **1998**, *83*, 1642.
- (14) Link, S.; Scholl, A.; Jacquemin, R.; Eberhardt, W. *Solid State Commun.* **2000**, *113*, 689.
- (15) Long, J. P.; Chase, S. J.; Kabler, M. N. *Chem. Phys. Lett.* **2001**, *347*, 29.
- (16) Long, J. P.; Chase, S. J.; Kabler, M. N. *Phys. Rev. B* **2001**, *64*, 205415.
- (17) Ton-That, C.; Shard, A. G.; Egger, S.; Dhanak, V. R.; Welland, M. E. *Phys. Rev. B* **2003**, *67*, 155415.
- (18) Benning, P. J.; Stepniak, F.; Weaver, J. H. *Phys. Rev. B* **1993**, *48*, 9086.
- (19) Hunt, M. R. C.; Rudolf, P.; Modesti, S. *Phys. Rev. B* **1997**, *55*, 7889.
- (20) Yang, W. L.; Brouet, V.; Zhou, X. J.; Choi, H. J.; Louie, S. G.; Cohen, M. L.; Kellar, S. A.; Bogdanov, P. V.; Lanzara, A.; Goldoni, A.; Parmigiani, F.; Hussain, Z.; Shen, Z.-X. *Science* **2003**, *300*, 303.
- (21) Brouet, V.; Yang, W. L.; Zhou, X. J.; Choi, H. J.; Louie, S. G.; Cohen, M. L.; Goldoni, A.; Parmigiani, F.; Hussain, Z.; Shen, Z. X. *Phys. Rev. Lett.* **2004**, *93*, 197601.
- (22) Brambilla, A.; Giovannelli, L.; Vilmercati, P.; Cattoni, A.; Biagioni, P.; Goldoni, A.; Finazzi, M.; Du , L. *J. Electron Spectrosc. Relat. Phenom.* **2005**, *144-147*, 803.
- (23) Dutton, G.; Zhu, X.-Y. *J. Phys. Chem. B* **2002**, *106*, 5975.
- (24) Dutton, G.; Pu, J.; Truhlar, D. G.; Zhu, X.-Y. *J. Chem. Phys.* **2003**, *118*, 4337.
- (25) Dutton, G.; Zhu, X.-Y. *J. Phys. Chem. B* **2004**, *108*, 7788.
- (26) Dutton, G.; Quinn, D. P.; Lindstrom, C. D.; Zhu, X.-Y. *Phys. Rev. B* **2005**, *72*, 045441.
- (27) Fauster, Th.; Steinmann, W. In *Photonic Probes of Surfaces*; Halevi, P., Ed.; Elsevier: Amsterdam, 1995.
- (28) Miller, A. D.; Gaffney, K. J.; Liu, S. H.; Szymanski, P.; Garrett-Roe, S.; Wong, C. M.; Harris, C. B. *J. Phys. Chem. A* **2002**, *106*, 7636.
- (29) Lingle, R. L.; Ge, N.-H.; Jordan, R. E.; McNeill, J. D.; Harris, C. B. *Chem. Phys.* **1996**, *205*, 191.
- (30) Tzeng, C.-T.; Lo, W.-S.; Yuh, J.-Y.; Chu, R.-Y.; Tsuei, K.-D. *Phys. Rev. B* **2000**, *61*, 2263.
- (31) Although this feature overlaps with minor peaks of Ag, signal from the substrate is attenuated quickly with increasing C_{60} coverage. Auger is not appropriate for detecting very small fractions of a C_{60} monolayer on Ag, but it is reliable in determining when a complete monolayer has been grown.
- (32) Argile, C.; Rhead, G. E. *Surf. Sci. Rep.* **1989**, *10*, 277.
- (33) Tjeng, L. H.; Hesper, R.; Heessels, A. C. L.; Heeres, A.; Jonkman, H. T.; Sawatzky, G. A. *Solid State Commun.* **1997**, *103*, 31.
- (34) Nakamura, A.; Ichida, M.; Yajima, T.; Shinohara, H.; Saitoh, Y. *J. Lumin.* **1996**, *66*, 383.
- (35) Shirley, D. A. *Phys. Rev. B* **1972**, *5*, 4709.
- (36) Miller, T.; Hansen, E. D.; McMahon, W. E.; Chiang, T.-C. *Surf. Sci.* **1997**, *376*, 32.
- (37) Haddon, R. C.; Brus, L. E.; Raghavachari, K. *Chem. Phys. Lett.* **1986**, *125*, 459.
- (38) Fowler, P. W.; Woolrich, J. *Chem. Phys. Lett.* **1986**, *127*, 78.
- (39) Ozaki, M.; Takahashi, A. *Chem. Phys. Lett.* **1986**, *127*, 242.

- (40) Guizzetti, G.; Marabelli, F.; Patrini, M.; Capozzi, V.; Lorusso, G. F.; Minafra, A.; Manfredini, M.; Milani, P. *Phys. Status Solidi B* **1994**, 183, 267.
- (41) Wertheim, G. K.; Buchanan, D. N. E.; Chaban, E. E.; Rowe, J. E. *Solid State Commun.* **1992**, 83, 785.
- (42) Shirley, E. L.; Louie, S. G. *Phys. Rev. Lett.* **1993**, 71, 133.
- (43) Moret, R. *Phys. Rev. B* **1993**, 48, 17619.
- (44) Dresselhaus, M. S.; Dresselhaus, G. *Annu. Rev. Mater. Sci.* **1995**, 25, 487.
- (45) Hoffman, R. *Solids and Surfaces: A Chemist's View of Bonding in Extended Structures*; VCH Publishers: Weinheim, 1988; pp 5–10.
- (46) Frisch, M. J.; Trucks, G. W.; Schlegel, H. B.; Scuseria, G. E.; Robb, M. A.; Cheeseman, J. R.; Zakrzewski, V. G.; Montgomery, J. A., Jr.; Stratmann, R. E.; Burant, J. C.; Dapprich, S.; Millam, J. M.; Daniels, A. D.; Kudin, K. N.; Strain, M. C.; Farkas, O.; Tomasi, J.; Barone, V.; Cossi, M.; Cammi, R.; Mennucci, B.; Pomelli, C.; Adamo, C.; Clifford, S.; Ochterski, J.; Petersson, G. A.; Ayala, P. Y.; Cui, Q.; Morokuma, K.; Rega, N.; Salvador, P.; Dannenberg, J. J.; Malick, D. K.; Rabuck, A. D.; Raghavachari, K.; Foresman, J. B.; Cioslowski, J.; Ortiz, J. V.; Baboul, A. G.; Stefanov, B. B.; Liu, G.; Liashenko, A.; Piskorz, P.; Komaromi, I.; Gomperts, R.; Martin, R. L.; Fox, D. J.; Keith, T.; Al-Laham, M. A.; Peng, C. Y.; Nanayakkara, A.; Challacombe, M.; Gill, P. M. W.; Johnson, B.; Chen, W.; Wong, M. W.; Andres, J. L.; Gonzalez, C.; Head-Gordon, M.; Replogle, E. S.; Pople, J. A. *Gaussian 98*, Revision A.11.4; Gaussian, Inc.: Pittsburgh, PA, 2002.
- (47) Wang, L.-L.; Cheng, H.-P. *Phys. Rev. B* **2004**, 69, 165417.
- (48) Wu, J.; Shen, Z.-X.; Dessau, D. S.; Cao, R.; Marshall, D. S.; Pianetta, P.; Lindau, I.; Yang, X.; Terry, J.; King, D. M.; Wells, B. O.; Elloway, D.; Wendt, H. R.; Brown, C. A.; Hunziker, H.; de Vries, M. S. *Physica C* **1992**, 197, 251.
- (49) Wertheim, G. K. *Phys. Rev. B* **1995**, 51, 10248.